## PAPER

Check for updates

# Investigation of Mn²⁺ dopant-induced crystal defects in photoactive CuSe nanosheets for enhanced visible-NIR range absorption and natural solar-driven photocatalysis

Vikas Kumar,[a] Jai Prakash, [ID] *[bd] Mahmoud Abid,[c] Mikhael Bechelany, [ID] [ce] Hendrik Christoffel Swart [ID] [d] and Awnish Kumar Tripathi*[a]

Limited light absorption and inefficient charge separation remain key challenges in achieving effective natural solar-driven photocatalysis using low-bandgap CuSe nanosheets (NSs). Introducing crystal defects within a certain concentration range has been recognized as an effective strategy to tackle these issues and to design a high-performance photocatalyst. Herein, Mn²⁺ is uniformly incorporated into the CuSe lattice, inducing crystal defects, resulting in efficient natural solar spectrum-driven photocatalysis. Photoluminescence (PL) spectroscopy revealed a systematic broadening in the full width at half maximum (FWHM) of defect-related emissions with increasing concentration of Mn-dopants, indicating the formation of defect states. Meanwhile, the conventional absorption spectrum indicated that without sacrificing the band gap, Mn-doped CuSe NSs exhibit improved visible and NIR-1 range absorption compared with the undoped CuSe NSs. Photocatalytic performance investigations, using methylene blue (MB) as a model dye, demonstrated a significant performance improvement. Results demonstrated that CuSe NSs with 9% Mn-doping showed 100% degradation with a degradation rate constant of 0.07 min⁻¹, which was approximately 2 times that of the undoped CuSe NSs. This significant improvement in the degradation efficiency suggests that the Mn-induced crystal defects hold significant promise for the effectiveness of CuSe NSs in natural solar spectrum-driven photocatalysis.

## 1. Introduction

In recent years, copper selenide (CuSe), a transition metal chalcogenide, has attracted significant attention due to its high stability, abundant availability of constituent elements, and visible-NIR light activity, making it a promising candidate for natural solar-driven photocatalysis.[1] Although CuSe exists in various stoichiometric and non-stoichiometric compositions with different crystal phases, the hexagonal crystal phase of CuSe has garnered significant attention.[2] Its low band gap provides a favorable environment for exploring its photo-catalytic potential, making it a promising candidate for advancing towards an effective solar energy conversion technology for a sustainable future. Unfortunately, the reliability of

these broad spectrum-active photocatalysts persistently remains a concern. Although its low band gap makes CuSe feasible for complete solar spectrum absorption, it also promotes the rapid recombination of electron–hole pairs, limiting its effectiveness in photocatalytic applications.[3] As a result, CuSe generally exhibits lower photocatalytic efficiency than conventional photocatalysts such as TiO₂ and ZnO.[4–6]

An effective approach to reducing the recombination rate of photogenerated electron–hole pairs involves two main strategies: (i) creating defects in the base lattice or (ii) forming a heterojunction by combining the base semiconductor with another suitable material. Firstly, the crystal defects modify the electronic band structure of the semiconductor by creating energy levels as trapping sites for the photogenerated charge carriers, effectively reducing the probability of electron–hole recombination.[7] This process ensures that the charge carriers remain separated for a longer duration, thereby improving the overall photocatalytic performance. Secondly, in the case of heterojunction fabrication, particularly Z-scheme hetero-junctions (notably p-n heterojunctions), the alignment of band edges can create an induced electric field near the junction, suppressing the charge-carrier recombination and improving the efficiency.[8] Both the strategies have been extensively

*[a]Department of Physics, National Institute of Technology Kurukshetra, Kurukshetra 136119, India. E-mail: awnish1982@nitkkr.ac.in*

*[b]Department of Chemistry, National Institute of Technology Hamirpur, Hamirpur, H. P., 177005, India. E-mail: jaip@nith.ac.in*

*[c]Institut Européen des Membranes, IEM, UMR 5635, Univ. Montpellier, ENSCM, CNRS, 34095 Montpellier, France*

*[d]Department of Physics, University of Free State, Bloemfontein ZN 9300, South Africa*

*[e]Functional Materials Group, Gulf University for Science and Technology, Mubarak Al-Abdullah, 32093, Kuwait*

investigated and reported by numerous research groups, demonstrating their effectiveness in suppressing the charge-carrier recombination and improving the photocatalytic efficiency.[7,9]

From a fundamental perspective, introducing defects within the semiconductor's lattice is often regarded as a more effective strategy for designing photocatalysts. This approach offers several advantages: (i) the precise band gap engineering improves optical absorption; (ii) it preserves the intrinsic properties of the material, which is often compromised in composites; (iii) it involves a simpler fabrication process; and (iv) it provides greater stability compared to composites. One practical approach to creating these energy levels is by introducing dopant ions into the host lattice.[10] Although this strategy creates an optimal environment for trapping photogenerated electron–hole pairs, the choice of a suitable dopant ion is crucial for achieving effective modifications in the crystal lattice. When choosing a suitable dopant, several factors must be considered. First, the ionic radius of the dopant ion should closely match that of the ions in the host lattice to ensure structural compatibility. Second, the dopant's oxidation states must be stable because unstable oxidation states can lead to charge imbalances, which may disrupt the lattice structure, causing unwanted phase transitions. For example, preserving the hexagonal crystal structure for CuSe is particularly important, as our earlier studies have shown that this phase exhibits superior photocatalytic performance.[11] Any phase transition could compromise the CuSe's photocatalytic efficiency.

Among the various transition metal ions considered, manganese (Mn) stands out as a particularly suitable choice for doping the CuSe lattice.[12] Unlike cobalt and iron, having stable $Co^{3+}$ and $Fe^{3+}$ states, previous studies have shown that these ions can induce phase transitions and alter the chemical composition due to charge imbalances.[11,13] Contrary to these, Mn offers significant advantages. $Mn^{2+}$ has a half-filled ([Ar] $4s^2$ $3d^5$) orbital configuration that is expected to replace $Cu^{2+}$ due to their comparable ionic radii.[14] This stable electronic configuration minimizes disruptions to the selenium ($Se^{2-}$) reticulum in the CuSe host lattice, reducing the likelihood of charge imbalances. Beyond these fundamental considerations, theoretical modeling underscores $Mn^{2+}$ as a potential dopant for improving the photocatalytic performance of different photocatalysts.[15,16] Therefore, considering $Mn^{2+}$ as a key dopant and nanosheets (NSs) as an effective nanoarchitecture for the CuSe photocatalyst,[2] the present investigation reveals the impact of $Mn^{2+}$ doping on the photocatalytic performance of CuSe NSs. Herein, CuSe NSs with varying $Mn^{2+}$ doping concentrations were synthesized, and its impact on the structural and optical properties of the CuSe NSs were investigated to ultimately assess their influence on the photocatalytic performance of the CuSe photocatalyst. We are optimistic that these findings will facilitate the practical implementation of the CuSe photocatalyst for large-scale natural solar-driven photocatalysis, while also contributing scientifically by providing insights into the effects of $Mn^{2+}$ doping on the structural and optical properties of CuSe semiconductor materials.

## 2. Experimental section

### 2.1 Materials

Analytic grade 99% pure cupric chloride dihydrate ($CuCl_2 \cdot 2H_2O$), 99% pure sodium selenite ($Na_2SeO_3$), 99.5% pure manganese chloride ($MnCl_2$), 99.5% pure tartaric acid ($C_4H_6O_6$), and hydrazine hydride ($N_2H_4$ $H_2O$ (60% aqueous solution) were used as starting materials, complexing and reducing agent, respectively. All reagents were obtained from Loba Chemical and used without any further purification.

### 2.2 Synthesis

All samples were prepared using the one-step hydrothermal method. A schematic diagram representing different steps involved in a typical synthesis process are presented in Fig. S1. In beaker A, copper chloride (0.2 M) and tartaric acid (0.2 M) were dissolved in 30 mL of distilled water. To achieve varying doping concentrations, specific amounts of $MnCl_2$ (1%, 3%, 5%, 7%, 9%, and 11% molar ratio relative to copper chloride) were added to the solution under continuous stirring (~600 rpm) at room temperature (~27 °C). In beaker B, a solution of sodium selenite (0.2 M) was prepared in 30 mL of distilled water under constant stirring (~600 rpm at room temperature), followed by the dropwise addition of 5 mL hydrazine (reducing agent). The solutions obtained in beakers A and B were mixed to obtain a dark brown color mixture. The pH of the mixture was monitored and set to pH 7 by adding aqueous (2 M) HCl.[2] After 30 min of magnetic stirring, the solution was transferred to a Teflon-lined stainless steel autoclave, and maintained at 180 °C for 4 h. Once the reaction was completed, the autoclave was allowed to cool naturally at room temperature. The resulting black precipitates were purified using a centrifugation-based washing protocol. The collected samples were transferred into 50 mL centrifuge tubes, filled with deionized (DI) water, and thoroughly mixed. The tubes were then centrifuged at 7500 rpm for 5 min. After centrifugation, the supernatant was carefully decanted, and the settled black powder was retained. This washing process was repeated 5–6 times to effectively remove any water-soluble byproducts and residual impurities. The collected samples were dried at 85 °C for 12 h in a hot air oven. The final products, with labels corresponding to different Mn-doping percentages as undoped CuSe, 1% Mn–CuSe, 3% Mn–CuSe, 5% Mn–CuSe, 7% Mn–CuSe, 9% Mn–CuSe, and 11% Mn–CuSe, were obtained for further characterization. A detailed description of the various characterization tools used to analyze the structural, optical, and photocatalytic properties of the synthesized photocatalysts is included in the SI.

## 3. Result and discussion

### 3.1 Crystal structure, morphology and composition analysis

The phase purity and crystalline nature of the prepared CuSe-based photocatalysts were investigated using the XRD technique. Fig. 1 illustrates the as-obtained XRD diffraction patterns of the prepared undoped and $Mn^{2+}$-doped CuSe NSs. As indexed in Fig. 1, prominent diffraction peaks were observed at 26.43°,
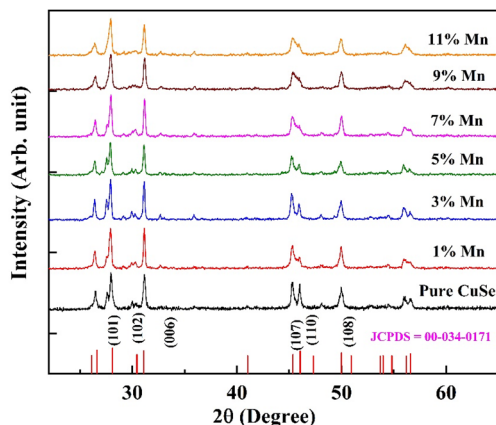
Fig. 1   XRD patterns of the prepared pure CuSe and Mn-doped CuSe samples.

27.89°, 31.17°, 45.30°, 46.03°, 50.05°, 56.03°, and 56.58° corresponding to the (101), (102), (006), (107), (110), (108), (203), and (116) planes, respectively, of the hexagonal crystal phase of CuSe, matching with JCPS card no. 034-0171.[2] No secondary phases corresponding to Mn-containing compounds were detected in the XRD patterns of Mn-doped CuSe NSs, indicating the absence of any segregated Mn-based phases. However, a slight shift in the principal diffraction peaks (Fig. S2) was observed upon Mn doping, which can be attributed to Vegard's law.[17] This law suggests that the incorporation of dopant ions into the host lattice does not produce distinct diffraction peaks, but can lead to a minor shift in the existing peaks due to changes in the lattice parameters.[18,19] The observed peak shift for the Mn-doped CuSe nanoparticles is in excellent agreement with the work of Patel *et al.*.[20] Furthermore, it is consistent with the substitutional incorporation of dopant-ions into the CuSe lattice, supporting the successful integration of Mn-ions in the CuSe matrix.

The influence of $Mn^{2+}$ doping on the crystallinity of CuSe was evaluated by estimating the crystallite size ($D$) of the prepared nanostructures, using the well-known Scherrer equation (eqn (1)), for the most intense (102) plane:[2]

$$D = \frac{0.9\lambda}{\beta \cos \theta} \tag{1}$$

where $\lambda$, $\beta$, and $\theta$ are the X-ray wavelength (Cu K$\alpha$ = 1.54 Å), full width half maxima (FWHM) of the peak, and the diffraction angle, respectively. The instrumental peak broadening was calibrated using the standard Si (111) peak, and was accounted for during the accurate estimation of FWHM.[21] Furthermore, the average crystallite size was estimated using the Scherrer method, while the Halder–Wagner (H–W) method was employed to calculate the lattice strain induced by Mn doping. A detailed justification for the choice of the H–W method over alternative approaches and detailed methodology (H–W method) has been thoroughly discussed elsewhere in the literature.[11,22] The H–W plots used to estimate the crystallographic parameters are presented in Fig. S3, while the parameters derived from both the Scherrer and HW methods are

summarized in Table 1. Notably, the crystallite size values obtained from both methods exhibit a similar trend, with minor differences in magnitude. This variation arises because the Scherrer method attributes the FWHM solely to the crystallite size, whereas the H–W method accounts for both crystallite size and microstrain contributions.[22] As a result, a slight deviation in crystallite size estimates is expected. The average crystallite size, calculated using eqn (1), falls in the range of 22–35 nm, indicating improved crystallinity and the presence of dopant-induced lattice strain in Mn-doped CuSe NSs.

Any alterations in lattice parameters is expected to substantially impact the energy dispersion relation ($E$ vs. $k$) within the Brillouin zone, ultimately affecting the carrier transport and optical absorption properties of the given photocatalyst.[22] Therefore, to examine the effect of $Mn^{2+}$ doping on the CuSe lattice, the lattice parameters ($a$ & $c$) of the synthesized samples were determined using eqn (2) and (3), given as:[2]

$$2d_{hkl}\sin \theta = n\lambda \tag{2}$$

$$\frac{1}{d_{hkl}^2} = \frac{4}{3}\left(\frac{h^2 + hk + k^2}{a^2}\right) + \frac{l^2}{c^2} \tag{3}$$

where $a$, $c$, and $d_{hkl}$ represent the lattice parameters and interplanar spacing corresponding to the ($h\,k\,l$) plane, respectively. The calculated lattice parameters using eqn (2) and (3) are summarized in Table 1. The variation of the aspect ratio ($c/a$) with the dopant concentration is also shown in Table 1. It demonstrates that as the doping concentration increases, the lattice constants (which are proportional to the ionic radii) change slightly without disturbing the aspect ratio ($c/a$), which confirms that $Mn^{2+}$ incorporation in CuSe hardly affects the overall crystal cage of the CuSe lattice.[23]

The morphological characteristics of the synthesized photocatalysts were examined using both FESEM and TEM. For the sake of brevity, the as-obtained FESEM images of pure CuSe and 9% Mn-doped CuSe NSs (identified as the most effective photocatalyst, as discussed later) are presented in Fig. 2(a and d), whereas, for all other samples, FESEM images have been provided in the SI (Fig. S4). The FESEM images exhibited a well-defined nanosheet-like morphology. Importantly, the incorporation of $Mn^{2+}$ into the CuSe structure did not result in any significant alteration in the overall morphology/nanostructural design, indicating that $Mn^{2+}$ ions were successfully incorporated into the lattice without disrupting the NSs morphology. To further validate the structural features, TEM analysis was conducted. The TEM images presented in Fig. 2(b and e) confirm the NSs morphology of the synthesized CuSe photocatalysts. The selected area electron diffraction (SAED) patterns and interplanar spacings, estimated from the HRTEM analyses shown in the insets of Fig. 2(b, d, c and f), respectively, are consistent with the hexagonal crystal structure. The retention of the NSs morphology following $Mn^{2+}$ doping indicates that the dopant ions are successfully incorporated into the CuSe lattice without significantly altering the structural features.

The purity and composition of the prepared photocatalysts were analyzed using EDS and XPS spectroscopy. The obtained EDS spectra for the prepared undoped and Mn-doped CuSe

**Table 1** Structural parameters calculated from XRD analysis. The instrumental peak broadening[21] was considered for the calculations using crystalline Si (1 1 1) as a standard

| Doping % | Crystallite size (Å) | | Lattice strain ($\varepsilon \times 10^{-3}$) | $a$ (Å) | $c$ (Å) | $c/a$ |
|---|---|---|---|---|---|---|
| | Scherrer method | H–W method | | | | |
| Pure CuSe | 22.15 ± 0.58 | 13.36 ± 1.21 | 2.9 | 3.98 | 17.23 | 4.33 |
| 1% | 25.78 ± 0.24 | 13.97 ± 0.94 | 4.5 | 3.97 | 17.22 | 4.34 |
| 3% | 36.89 ± 1.05 | 14.70 ± 1.21 | 4.7 | 3.97 | 17.23 | 4.34 |
| 5% | 37.38 ± 1.51 | 15.12 ± 0.57 | 5.1 | 3.98 | 17.20 | 4.33 |
| 7% | 37.21 ± 1.97 | 14.32 ± 1.68 | 4.5 | 3.97 | 17.20 | 4.33 |
| 9% | 22.57 ± 0.22 | 13.66 ± 0.87 | 4.8 | 3.97 | 17.21 | 4.33 |
| 11% | 21.53 ± 0.58 | 12.81 ± 1.45 | 5.1 | 3.98 | 17.20 | 4.33 |

photocatalysts are shown in Fig. S5. The analysis reveals the presence of Cu, Se, and Mn, with no additional peaks, indicative of the purity of the CuSe NSs. To counter the possibility of cluster formation of the dopant ions,[24] the EDS mapping has been conducted and gives the uniform distribution of Mn-ions (Fig. S6) in the CuSe lattice. Although the EDS analysis gives the primary indication of the presence of Mn-dopant, further investigation is necessary to investigate the exact oxidation state of the Mn-dopant and to clarify the chemical composition of the prepared NSs.[25] Therefore, XPS was performed as a confirmatory analysis for the chemical situation of elements in the product. The obtained full-range XPS spectrum for 5% Mn doped CuSe NSs is shown in Fig. 3(a), indicating the existence of Cu, Se, Mn, O, and C. The observed C 1s peak originates from the carbon tape used during the XPS measurements. Prior to data interpretation, it is standard practice to calibrate the acquired XPS spectra. The adventitious carbon C 1s peak is commonly used as a reference point for this purpose, with its binding energy (BE) typically reported in the range of 284.60–284.80 eV in the literature.[26,27] In accordance with standard convention and our

previous publication,[28] all spectra in this study were calibrated using the C 1s peak positioned at 284.70 eV before further analysis. The observed oxygen is attributed to adsorbed atmospheric oxygen.[29] Fig. 3(b–d) show the high-resolution XPS spectra of Cu, Se and Mn, respectively. The binding energies at 951.8 eV, 931.9 eV, 55.4 eV, and 54.6 eV were assigned to Cu $2p_{1/2}$, Cu $2p_{3/2}$, Se $3d_{3/2}$, and Se $3d_{5/2}$, respectively.[30] Moreover, the Cu 2p XPS spectrum displays a satellite peak between 940 and 945 eV, further confirming the existence of $Cu^{2+}$ in the prepared product.[29] The XPS spectrum of Se 3d shows that the binding energy of Se$3d_{5/2}$ is 54.0 eV, demonstrating the existence of $Se^{2-}$ in the synthesized product,[31] while the presence of additional Se–O peaks at 58–60 eV (Fig. 3(c)) may be due to the surface oxidation of the selenide after prolonged exposure of the sample in air.[29] In Fig. 3(a), a characteristic feature within the 600–660 eV region corresponds to the Mn 2p binding energies, which are well reported in the literature.[32,33] Furthermore, the high-resolution XPS spectrum (Mn 2p, Fig. 3(d)) displays two distinct peaks at ~641 eV and 653 eV. The peak at ~641 eV is attributed to Mn $2p_{3/2}$. Meanwhile, the other peak observed at
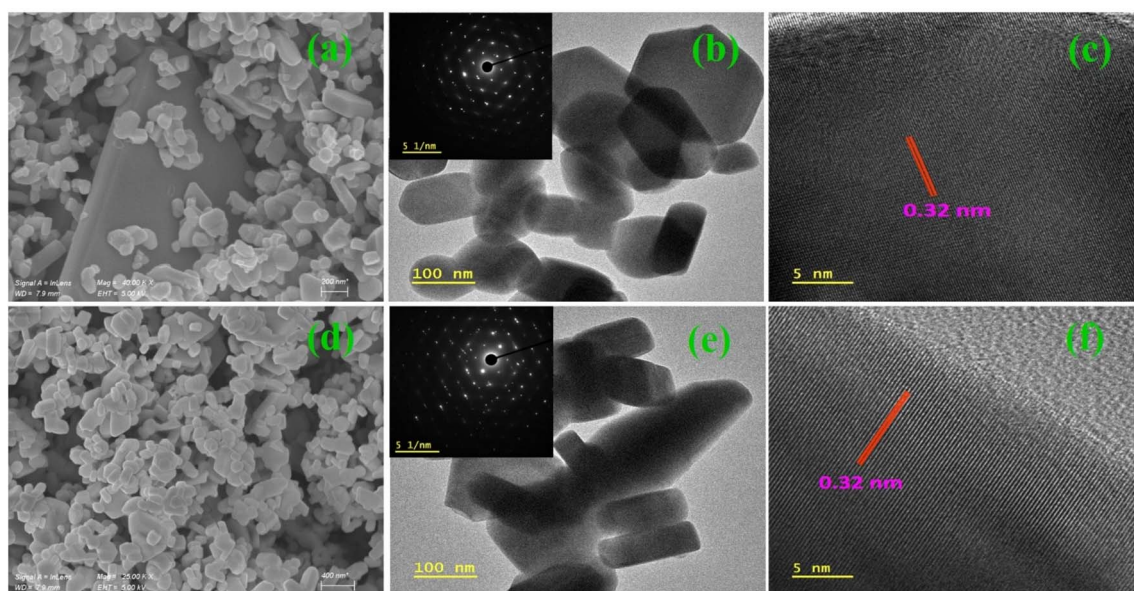


**Fig. 2** FESEM images, HRTEM images (with insets showing the corresponding SAED patterns), and interplanar spacing analysis (from HRTEM), respectively, of (a–c) pure CuSe and (d–f) 9% Mn-doped CuSe.
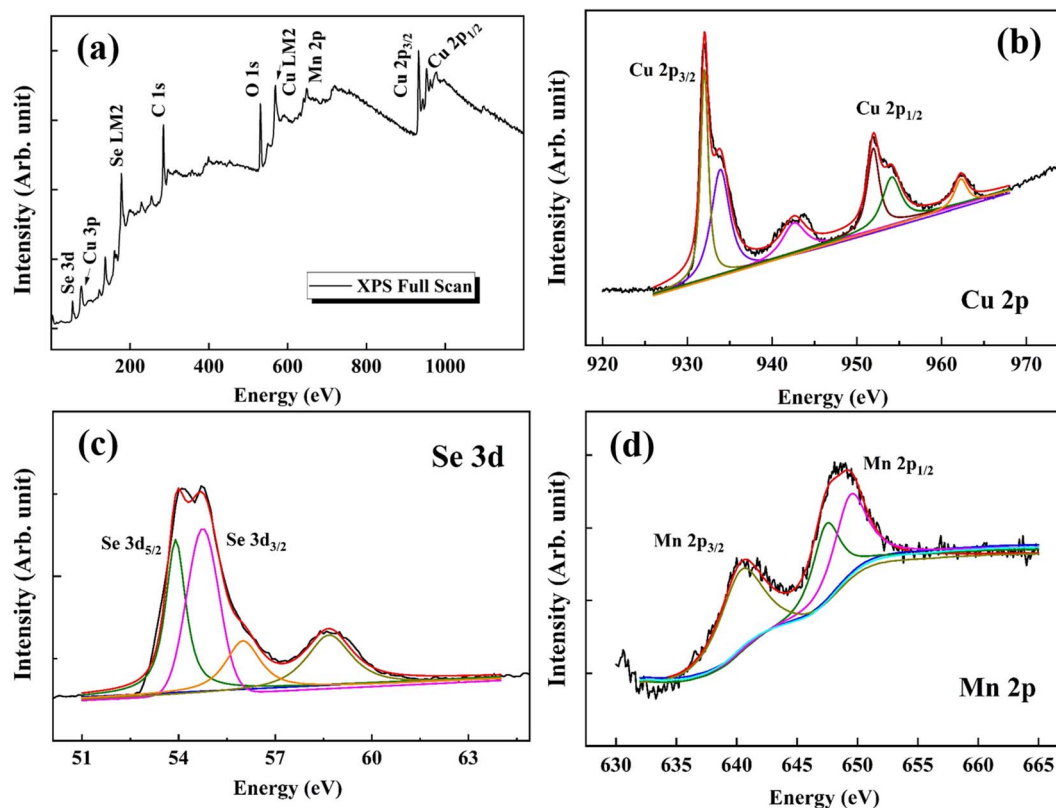
**Fig. 3** The XPS scan for 5% Mn-doped CuSe: (a) XPS elemental full survey, (b) high-resolution Cu 2p XPS survey, (c) high-resolution Se 3d XPS survey, and (d) high-resolution Mn 2p XPS survey.

~653 eV (with an energy difference of ~12 eV) corresponds to the Mn $2p_{1/2}$ level, which is a well-established signature of the $Mn^{2+}$ oxidation state, as extensively reported in the literature.[34,35] This confirms the successful substitutional incorporation of $Mn^{2+}$ ions into the CuSe lattice. The absence of peaks near ~643 eV, which are typically associated with higher oxidation states (such as $Mn^{3+}$ or $Mn^{4+}$), further supports the predominance of Mn in the +2 oxidation state. Consistent with Cheng et al.'s findings[30] and reported findings for $Mn^{2+}$-induced characteristics,[36] XPS measurements and analysis confirm the presence of $Cu^{2+}$ and $Se^{2-}$ in the resulting product, indicating a CuSe stoichiometry and confirming the presence of $Mn^{2+}$-dopants in the host lattice. These XPS findings align well with the results from XRD and EDS, collectively providing robust evidence regarding the phase and stoichiometry of the synthesized materials.

## 3.2 Optical properties

**3.2.1 UV-vis-NIR absorption spectroscopy.** To study the absorption behavior and investigate the impact of $Mn^{2+}$-doping on the energy band gap ($E_g$) values of CuSe NSs, the room temperature absorption spectra were recorded in the range of 300–1000 nm. Typically, the absorption measurements were conducted using DI water as the reference. The CuSe NSs were homogenously dispersed in DI water before conducting the measurements. The obtained absorption spectra for undoped

and $Mn^{2+}$-doped CuSe NSs are shown in Fig. 4(a). The obtained spectra reveal that the undoped CuSe NSs exhibit absorption across the visible and NIR-1 region of the solar spectrum. For $Mn^{2+}$-doped CuSe NSs, a significant change in absorption intensity was observed, while there was no notable shift in the absorption edge. These results indicate that the introduction of $Mn^{2+}$ dopants does not significantly affect the band edge positions of the CuSe NSs. The $E_g$ values for the prepared CuSe photocatalysts were estimated using eqn (4):

$$(\alpha h\upsilon)^n = A(h\upsilon - E_g) \tag{4}$$

where $E_g$ is the separation between the valence band (VB) edge and conduction band (CB) edge, $h\upsilon$ is the photon energy, $A$ is a proportionality constant, and $\alpha$ is the absorption coefficient. In the literature, different values of $n$ have been attributed to different types of optical transitions.[37] The band gap has been estimated by adopting the procedures suggested by Makuła et al.[38] For all the obtained absorption spectra, a linear Tauc plot for $n = 2$ was obtained, which has been well reported for the hexagonal crystal phase of CuSe.[39,40] It refers to the indirect band-to-band optical transition.[37] A typical Tauc plot for 9% $Mn^{2+}$-CuSe is shown in Fig. 4(b), while the estimated band gaps for the other CuSe photocatalysts are provided in the SI (Table S1). The estimated band gap values of the CuSe photocatalysts exhibit a small variation ranging from 1.67 eV to 1.74 eV, as shown in the inset of Fig. 4(b). This small change in the band
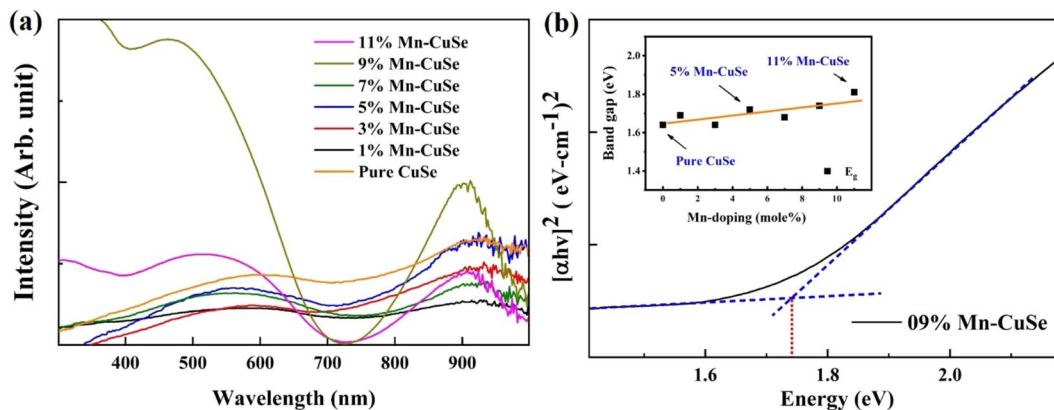
Fig. 4 (a) Obtained absorption spectra for the prepared Mn-doped CuSe photocatalysts. (b) Typical Tauc plot for the undoped CuSe NSs. The upper left inset shows the variations in $E_g$ for the CuSe photocatalyst with varying Mn-doping concentration.

gap of CuSe NSs might be due to the small change in the lattice parameters resulting from the $Mn^{2+}$ ion incorporation in the CuSe lattice. Theoretical insights suggest that changes in lattice parameters can critically impact the energy dispersion relation, $E$ vs. $k$, within the Brillouin zone. This alteration in $E$ vs. $k$ affects the material's optical absorption.[11] In a typical experiment, a slight variation in the lattice parameter was observed with $Mn^{2+}$ doping in CuSe NSs, as shown in Table 1. Ultimately, it leads to a small modulation in the band gap value of the CuSe NSs. Previous studies have consistently reported and explained the role of dopant ion-induced crystal defects in improving the absorption without sacrificing the band gap value.[41] In alignment with these findings, the absorption spectra of the $Mn^{2+}$-doped CuSe NSs (Fig. 4(a)) demonstrate improved absorption capability, indicating the enhanced natural solar-spectrum-like light-harvesting capability of CuSe NSs. In addition, the improved crystallinity for the CuSe crystal lattice with $Mn^{2+}$ might be the reason for the improved absorption behavior of the prepared $Mn^{2+}$-doped CuSe NSs.[42] The findings from the absorption spectra exhibit a strong correlation with the XRD analysis results, where the incorporation of $Mn^{2+}$ ions was observed to slightly alter the lattice parameters and crystallinity of the CuSe NSs. These structural modifications subsequently influence the optical properties of the CuSe NSs, as evidenced by modifying the absorption characteristics.

**3.2.2 Photoluminescence (PL) spectroscopy.** PL measurements were conducted to examine the luminescent properties and to assess the impact of $Mn^{2+}$ doping on these properties for CuSe NSs. All samples were excited using 405 nm excitation wavelength, and the spectrum was recorded by keeping an optimum slit width of the setup. The obtained PL spectra for the CuSe samples are shown in Fig. 5(a). It has been reported in the literature that for CuSe, the PL peak centered at 615 nm is attributed to the excitation of electrons from the VB to the CB, *i.e.*, band-to-band transition.[43–45] In a typical experiment, the emission peak aligns closely with the reported literature values, confirming the successful synthesis of impurity-free, hexagonal-phase CuSe.[46] Here, the PL spectra have been fitted using a standard double Gaussian function after subjecting it to

"Jacobian transformation".[47] As reported in the literature,[37] such treatment is crucial for correct interpretations, where a single material exhibits a broad range of PL emissions. A typical spectrum, subjected to this analysis, is also shown in Fig. 5(b), and the methodology of "Jacobian transformation" is discussed elsewhere in the literature.[48] For brevity, the Gaussian fitting of the PL spectrum for the 9% Mn-doped CuSe sample is shown in Fig. 5(b), while the deconvolution of the PL spectra for the other samples are presented in the SI (Fig. S7). The estimated parameters for all CuSe NSs are listed in Table 2. As shown in Fig. 5(b), the PL peak centered around 2.03 eV (610 nm) closely aligned with the reported emission and can be attributed to the band-to-band transition of CuSe NSs. Additionally, a shoulder peak appearing at ∼2.00 eV (620 nm) was observed. Consistent with the findings of Shitu *et al.*[49] and others,[45,46] this observed emission (∼2.00 eV) is attributed to defect-level emission, suggesting the presence of intrinsic point defects within the CuSe NSs. These defects, including copper vacancies, interstitials, and antisite defects, are usually localized at the surface of the CuSe NSs. These defect-induced emissions associated with Cu vacancies support the successful substitution of $Cu^{2+}$ ions by $Mn^{2+}$ dopants within the CuSe lattice. Similar observations were found for all $Mn^{2+}$-doped CuSe NSs (Fig. S7). Interestingly, the FWHM for the peak at 2.03 eV decreases from 4.21 meV to 3.15 meV. Meanwhile, for the peak at 1.99 eV, it increases from 1.64 meV to 4.42 meV with an increase in the $Mn^{2+}$ doping percentage in the CuSe NSs. This increase in the area under the 1.99–2.00 eV peak with $Mn^{2+}$ doping suggests an improvement in emission signals originating from surface defects. This trend shows an increase in crystal defects as the $Mn^{2+}$ ion concentration rises within the host material. It is worth noting in the literature[50] that such defects can act as trapping sites for photogenerated electron–hole pairs, thereby reducing their recombination rate. However, a more in-depth analysis of the PL signals is necessary to fully elucidate the role of these $Mn^{2+}$ dopant-induced surface defects in CuSe NSs on the recombination rate of CuSe NSs and open for further exploration by the scientific community.
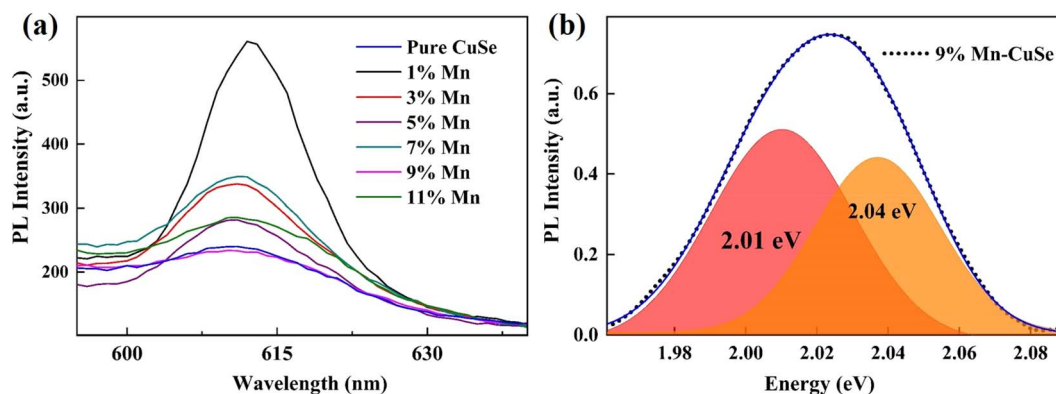
**Fig. 5** Gaussian function fit of the room temperature PL spectrum of (a) pure CuSe NSs (b) 9% Mn–CuSe NSs.

# 4. Photocatalytic performance

The photocatalytic performance of CuSe was evaluated under the illumination of a 300 watt halogen lamp used as a rich VIS-NIR radiation source. Here, MB is used as a model dye to investigate the photocatalytic performance of the prepared CuSe samples. The steps used in evaluating the photocatalytic performance follow the same methodology outlined in our previous publication.[2]

The obtained absorption spectra for the MB sample collected at different intervals of light irradiation, utilizing typically the undoped and 9% Mn–CuSe samples, are presented in Fig. 6(a). The prominent peak observed at ~664 nm corresponds to MB, and was used to estimate the degradation percentage at different intervals of light exposure. The observed decrease in peak intensity indicates a reduction in the MB concentration, revealing the photodegradation of MB in the presence of the utilized photocatalysts. The methodology adopted for determining the dye concentration from the absorption spectra is the same as that described in our previous publication.[11] To quantify these observations, the percentage degradation of dye concentration is calculated using the following relation:

$$\% \text{ Degradation} = \frac{C_0 - C}{C_0} \times 100 = \frac{\Delta C}{C_0} \times 100 \quad (5)$$

where $C_0$ is the initial concentration and $C$ is the concentration of the dye at the time of withdrawal of the sample. Moreover, a plot of $C/C_0$ for CuSe samples with varying Mn-doping concentrations is shown in Fig. 6(b). The key role of Mn

dopants in CuSe NSs affecting its photocatalytic performance was further checked by evaluating the rate constants, obtained by the following first-order rate equation:[51]

$$\ln \frac{C}{C_0} = -k_{app}t \quad (6)$$

where $k_{app}$ is the apparent first-order rate constant. The slope of linear fitted plot between $\ln(C/C_0)$ *vs. t*, provided in Fig. 6(c), provides the numerical measures of the rate constant for the photodegradation of MB in the presence of different CuSe photocatalysts. To facilitate a comprehensive understanding of the variation in the rate constant, the obtained rate constants for all prepared CuSe NSs are illustrated in Fig. 6(d). The results clearly indicate a significant difference among the rate constant values for CuSe NSs prepared with different concentrations of Mn-doping in the host material. The rate constant is highest for the sample prepared with 9% Mn doping, suggesting that this sample exhibits radical generation among all other samples. This significant change in the degradation rate constant upon Mn-doping can be attributed to notable alterations in its optical properties caused by the incorporation of Mn-ions into the host material. Interestingly, the degradation efficiency of the CuSe NSs photocatalyst exhibits a non-monotonic trend. It reaches a maximum at 9% Mn doping, beyond which a significant decline in the efficiency is observed. These results suggest that for the CuSe NSs, crystal defects induced by $Mn^{2+}$ ion incorporation influence the recombination rate. Up to a certain defect concentration, these defects promote charge carrier recombination. However, beyond this threshold, the defects appear to

**Table 2** Estimated peak position and corresponding FWHM for the obtained PL spectra of the prepared CuSe and Fe–CuSe photocatalysts

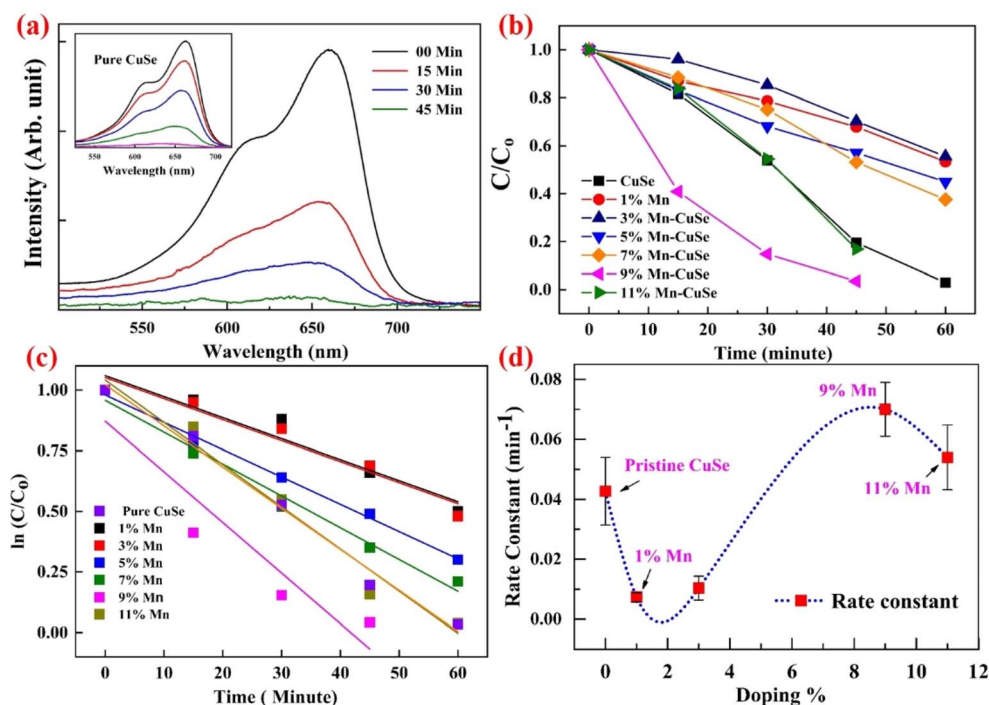| Sample | $P_1$ (eV) | FWHM | $P_2$ (eV) | FWHM | $\chi^2$ |
|---|---|---|---|---|---|
| Undoped CuSe | 1.99 | $0.0016 \pm 0.0001$ | 2.03 | $0.0421 \pm 0.0016$ | 0.99 |
| 1% Mn–CuSe | 1.99 | $0.0119 \pm 0.0026$ | 2.03 | $0.0362 \pm 0.0009$ | 0.99 |
| 3% Mn–CuSe | 2.00 | $0.0152 \pm 0.0021$ | 2.03 | $0.0361 \pm 0.0007$ | 0.99 |
| 5% Mn–CuSe | 2.00 | $0.0228 \pm 0.0027$ | 2.03 | $0.0287 \pm 0.0003$ | 0.99 |
| 7% Mn–CuSe | 2.00 | $0.0249 \pm 0.0021$ | 2.03 | $0.0353 \pm 0.0014$ | 0.99 |
| 9% Mn–CuSe | 2.01 | $0.0442 \pm 0.0019$ | 2.03 | $0.0193 \pm 0.0048$ | 0.99 |
| 11% Mn–CuSe | 2.01 | $0.0213 \pm 0.0009$ | 2.03 | $0.0034 \pm 0.0008$ | 0.99 |

Fig. 6 (a) Absorption spectra of the MB solution during the photo-degradation process for 9% Mn–CuSe NSs. The inset shows the absorption spectra for pure CuSe NSs. (b) Photocatalytic performance of the prepared photocatalyst for the photodegradation of MB under visible light irradiation. (c) Linear fitting in ln($C/C_0$) for the prepared photocatalysts. (d) Variation in the rate constant for the prepared photocatalysts.

suppress recombination, thereby improving the overall photocatalytic performance of the CuSe NSs. The estimated degradation percentage of 9% Mn-doped CuSe was observed to have the maximum degradation efficiency, reaching 100% in ~45 min under visible and NIR light irradiation.

## 4.2 Insight into the degradation mechanism

To explore the potential photocatalytic mechanism, we utilized the findings from a range of characterization methods, including VIS-NIR absorption spectroscopy, PL spectroscopy, and photocatalytic degradation study. A detailed investigation of the band edges is essential to evaluate the redox potential for the prepared CuSe photocatalyst. For the undoped CuSe photocatalyst, the valence band edge was determined through XPS valence band scans, as displayed in Fig. 7(a). The estimated band gap edges for the CuSe photocatalyst are shown in Fig. 7(c), which align well with the theoretically estimated band gap edges discussed in our previous publications.[2] These results help to investigate the potential oxidation and reduction pathways for photogenerated electron–hole pairs in CuSe NSs, providing constructive insights into the CuSe NS's redox behavior. Furthermore, to explore the generation and role of different radicals, we conducted radical trapping experiments. By analyzing undoped CuSe samples, we aimed to clarify the photocatalytic degradation mechanism, which can be extended to other prepared samples. A comprehensive analysis of the collected data enables us to propose a relevant degradation mechanism for the MB dye, visually represented in Fig. 7(c).

The results from absorption spectroscopy indicate that the prepared samples exhibit excellent absorption in the visible and NIR regions. This suggests that when the prepared CuSe NSs was irradiated with a 300 W halogen bulb (Vis-NIR light), the electrons from the valence band are elevated to the conduction band. The band edge estimated using XPS analysis reveals the ability of these redox potentials to produce hydroxyl radicals for the $O_2$ and $H_2O_2$ molecules. Therefore, these photo-generated electrons and holes react with oxygen and water molecules to generate $\cdot O_2^-$ and OH* radicals, respectively.[52,53] This process is feasible when the oxidation and reduction potentials of $O_2$ and $H_2O$, respectively, lie within the $E_g$,[39] as depicted in Fig. 7(b). Since the oxidation potential of holes for the synthesized CuSe is above the redox potential of $H_2O$,[3] the concentration of the OH* radicals would be nominal. As discussed earlier, MB degradation by VIS-NIR radiation was observed in the presence of $H_2O_2$. In the absence of $H_2O_2$, the photo-generated electrons and holes might not reduce $O_2$ to $\cdot O_2^-$ and $H_2O$ to OH* radicals, which are responsible for the MB molecules' degradation. In contrast, when $H_2O_2$ is added to the mixture, the dye degradation takes place as the $H_2O_2$ redox potential induces a favorable situation for free radical (OH*) generation. To evaluate the reactive species involved in the photocatalytic degradation of MB using CuSe NSs, radical trapping experiments were conducted. Isopropanol (IPA), ethylene diamine tetra acetic acid disodium salt (EDTA-2Na), and 1,4-benzoquinone (BQ) were used as scavengers for hydroxyl radicals (OH*), photogenerated holes ($h^+$), and superoxide radicals ($\cdot O_2^-$), respectively.[54] The estimated degradation percentages in the presence of different
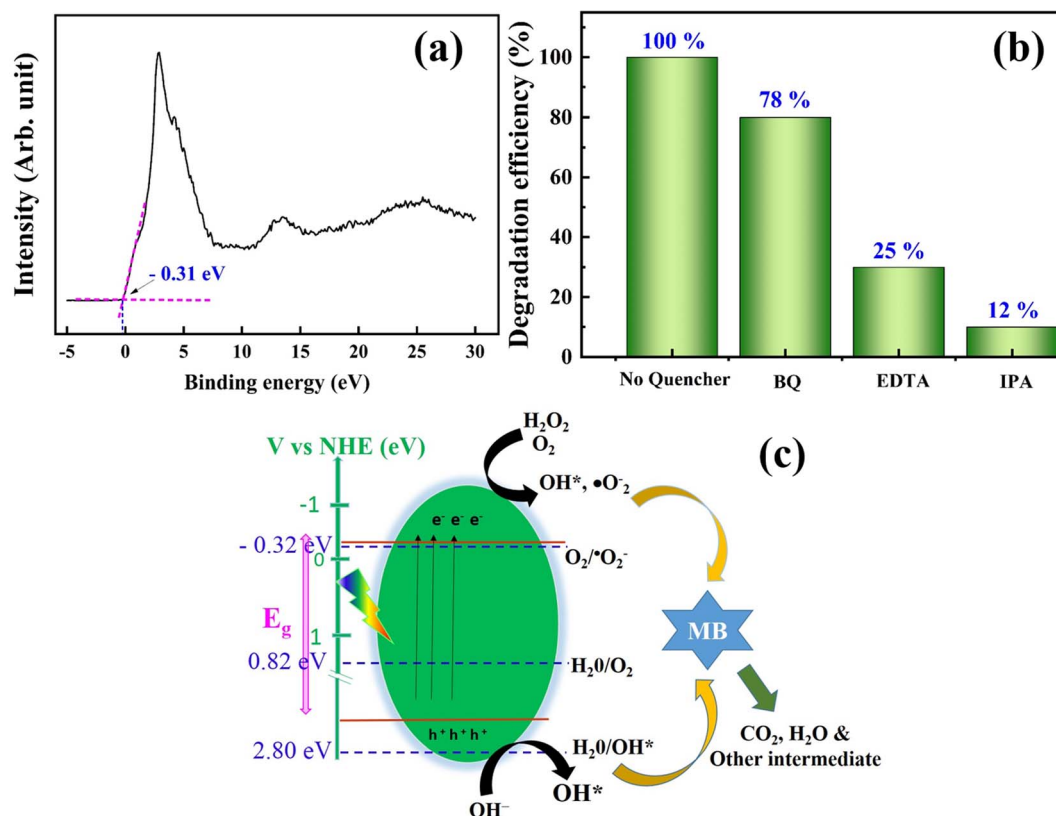
**Fig. 7** (a) Valence band XPS spectrum for undoped CuSe NSs. (b) Radicals trapping results for MB degradation using the undoped CuSe photocatalyst. (c) Proposed photocatalytic mechanism for the CuSe photocatalyst.

scavenging agents are shown in Fig. 7 (a). The results demonstrate an excellent correlation with previously reported outcomes in the literature.[2] The output suggests the significant role of $h^+$ and OH* in the degradation process. As a result, the crucial roles of these reactive species to the photocatalytic degradation of MB using the CuSe photocatalyst system were found in the following order OH* > $h^+$ > $\cdot O_2^-$.

The electrons in the VB of CuSe are elevated to CB by the absorption of photons with energy higher than the $E_g$ (threshold energy), leading to photo-generated charges. Finally, these abundant hydroxyl radicals (OH*) react with the dye to form $H_2O$, $CO_2$, and some other intermediates as major mineralization products.[40,55,56]

## 5. Conclusion

In summary, we have developed photoactive $Mn^{2+}$-doped CuSe NSs with tailored crystal defects to develop an efficient full-spectrum solar photocatalyst. Using a controlled hydrothermal doping approach, we systematically introduced $Mn^{2+}$ ions into the CuSe lattice, optimizing the defect concentrations to improve the photocatalytic performance. Our investigations reveal that these defects serve the following roles: (i) they improve light absorption by sacrificing the band gap, and (ii) they reduce the recombination rate of photogenerated electron–hole pairs, leading to superior photocatalytic activity compared

to undoped CuSe NSs. However, the outcomes reveal a critical threshold; beyond an optimal defect concentration, these same defects in CuSe NSs transform into recombination centers, ultimately degrading the photocatalytic activity. This dichotomy highlights the delicate balance required in defect engineering for solar energy applications, where optimal doping concentrations must simultaneously maximize charge separation while preserving sufficient redox capability. These findings provide crucial design principles for optimizing defect-mediated photocatalysts, paving the way for smarter material engineering in renewable energy technologies.

## Conflicts of interest

There are no conflicts to declare.

## Data availability

The data supporting this article have been included as part of the SI.

Details of experimental and characterization techniques, XRD analysis, Halder–Wagner plot, FESEM and EDS analysis, Tauc plots and fitting of PL spectra. See DOI: **https://doi.org/10.1039/d5na00372e**.

# References

1 C. M. Hessel, V. P. Pattani, M. Rasch, M. G. Panthani, B. Koo, J. W. Tunnell and B. A. Korgel, Copper selenide nanocrystals for photothermal therapy, *Nano Lett.*, 2011, **11**, 2560–2566.

2 V. Kumar, J. Prakash, S. K. Kansal and A. K. Tripathi, Tailoring the geometry of visible and near-infrared light active CuSe nanostructure for enhanced photocatalytic activity, *Nano-Struct. Nano-Objects*, 2024, **39**, 101276.

3 M. Nouri, R. Yousefi, N. Zare-Dehnavi and F. Jamali-Sheini, Tuning crystal phase and morphology of copper selenide nanostructures and their visible-light photocatalytic applications to degrade organic pollutants, *Colloids Surf., A*, 2020, **586**, 124196, DOI: 10.1016/j.colsurfa.2019.124196.

4 A. Chawla, A. Sudhaik, R. Kumar, P. Raizada, A. A. P. Khan, T. Ahamad, V.-H. Nguyen, R. Selvasembian, A. Kaushik and P. Singh, a Recent advances in synthesis methods and surface structure manipulating strategies of copper selenide (CuSe) nanoparticles for photocatalytic environmental and energy applications, *J. Environ. Chem. Eng.*, 2024, 113125.

5 N. Ghobadi, M.-R. Zamani Meymian and M. Fallah, Exploring secondary optical transitions: a study utilizing the DITM method, and enhanced photocatalytic properties in Ni-doped CuSE, *Sci. Rep.*, 2024, **14**, 7754.

6 Y. Yan, Y. Wu, Y. Wu, Z. Weng, S. Liu, Z. Liu, K. Lu and B. Han, Recent Advances of CeO$_2$-Based Composite Materials for Photocatalytic Applications, *ChemSusChem*, 2024, **17**, e202301778.

7 L. An and H. Onishi, Electron–hole recombination controlled by metal doping sites in NaTaO$_3$ photocatalysts, *ACS Catal.*, 2015, **5**, 3196–3206.

8 Y. Sun, T. Hu, H. Wang, Q. Wu, Y. Liu, S. Cheng, S. Chen, Y. Yu and L. Li, Design of dual Z-scheme heterojunction Ag/AgI@ Bi$_2$O$_2$CO$_3$/3DOM TiO$_2$ composite materials with solar-driven photocatalytic degradation and hydrogen production, *Int. J. Hydrogen Energy*, 2024, **90**, 710–722.

9 D. Pan, J. Jiao, Z. Li, Y. Guo, C. Feng, Y. Liu, L. Wang and M. Wu, Efficient Separation of Electron–Hole Pairs in Graphene Quantum Dots by TiO$_2$ Heterojunctions for Dye Degradation, *ACS Sustain. Chem. Eng.*, 2015, **3**, 2405–2413, DOI: 10.1021/acssuschemeng.5b00771.

10 L. Huang, G. He, Y. Yuan, T. C. Zhang, Y. Wang and S. Yuan, Trivalent Metal Ions (Al, Ga, In)-Doped TiO$_2$ for Enhanced Photocatalytic Desulfurization of H2S: Band Structure Regulation, Performance, and Mechanism, *Ind. Eng. Chem. Res.*, 2024, **63**, 7154–7165.

11 V. Kumar, J. Prakash, S. K. Kansal and A. K. Tripathi, Fe$^{3+}$-dopants mediated crystal structure modifications in photoactive CuSe nanosheets for achieving effective natural solar spectrum driven photocatalysis, *Phys. B*, 2025, 416968.

12 Q. R. Deng, X. H. Xia, M. L. Guo, Y. Gao and G. Shao, Mn-doped TiO$_2$ nanopowders with remarkable visible light photocatalytic activity, *Mater. Lett.*, 2011, **65**, 2051–2054.

13 V. Kumar, J. Prakash, H. C. Swart and A. K. Tripathi, Cobalt (Co) – doped photoactive CuSe nanosheets for improved NIR-1 range light absorption for effective full solar spectrum active photocatalysis, *Mater. Lett.*, 2025, **389**, 138349, DOI: 10.1016/j.matlet.2025.138349.

14 S. Masrat, R. Poolla, P. Dipak and M. B. Zaman, Rapid hydrothermal synthesis of highly crystalline transition metal (Mn & Fe) doped CuSe nanostructures: applications in wastewater treatment and room temperature gas sensing, *Surf. Interfaces*, 2021, **23**, 100973.

15 S. Wang, J. Ren, Z. Pan, Y. Su, B. Tian, J. Zhang and Q. Wang, Ab initio studies of the effects of Mn and intrinsic vacancy on the electronic, optical, water splitting properties of hematite Fe$_2$O$_3$ monolayer, *Opt. Mater.*, 2024, **148**, 114898.

16 X. Tan, H. Shao, T. Hu, G.-Q. Liu and S.-F. Ren, Theoretical understanding on band engineering of Mn-doped lead chalcogenides PbX (X= Te, Se, S), *J. Phys.: Condens. Matter*, 2015, **27**, 95501.

17 R. M. Kannaujiya, S. H. Chaki, A. J. Khimani, A. B. Hirpara, Z. R. Parekh, R. K. Giri, S. Patel and M. P. Deshpande, Effect of Sb doping on CVT grown SnTe single crystals electrical and thermal properties, *J. Mater. Sci.: Mater. Electron.*, 2022, **33**, 20823–20836.

18 A. J. Khimani, S. H. Chaki, M. P. Deshpande and J. P. Tailor, Study of indium and antimony incorporation into SnS$_2$ single crystals, *J. Cryst. Growth*, 2019, **507**, 180–188.

19 M. Elango, K. Gopalakrishnan, S. Vairam and M. Thamilselvan, Structural, optical and magnetic studies on non-aqueous synthesized CdS: Mn nanomaterials, *J. Alloys Compd.*, 2012, **538**, 48–55.

20 S. R. Patel, S. H. Chaki, R. K. Giri, A. J. Khimani, Y. H. Vaidya, P. Thakor, A. B. Thakkar and M. P. Deshpande, Pristine, Ni- and Zn-Doped CuSe Nanoparticles: An Antimicrobial, Antioxidant, and Cytotoxicity Study, *ACS Appl. Bio Mater.*, 2023, **6**, 2211–2225, DOI: 10.1021/acsabm.3c00090.

21 U. Holzwarth and N. Gibson, The Scherrer equation *versus* the "Debye-Scherrer equation,", *Nat. Nanotechnol.*, 2011, **6**, 534, DOI: 10.1038/nnano.2011.145.

22 K. Patel, G. K. Solanki, K. D. Patel and V. M. Pathak, X-ray diffraction analysis of hexagonal klockmannite cuse nanoparticles for photodetectors under UV light, *J. Phys. Chem. C*, 2021, **125**, 3517–3526, DOI: 10.1021/acs.jpcc.0c09353.

23 P. Kaur, S. Kaur, D. Arora, A. Kandasami and D. P. Singh, Correlation among lattice strain, defect formation and luminescence properties of transition metal doped ZnO nano-crystals prepared *via* low temperature technique, *Mater. Res. Express*, 2019, **6**, 115920.

24 Y. Wei, Y. Wu, J. Wang, Y.-H. Wu, Z. Weng, W.-Y. Huang, K. Yang, J.-L. Zhang, Q. Li and K.-Q. Lu, Rationally designed dual cocatalysts on ZnIn$_2$S$_4$ nanoflowers for photoredox coupling of benzyl alcohol oxidation with H$_2$ evolution, *J. Mater. Chem. A*, 2024, **12**, 18986–18992.

25 C. Yan, G. Chen, Y. Zhang, D. Chen, J. Pei and Z. Qiu, CuSe$_{1-x}$S$_x$ nanosheets with an ordered superstructure as anode materials for lithium-ion batteries, *New J. Chem.*, 2016, **40**, 6588–6592.

26 G. Greczynski and L. Hultman, Reliable determination of chemical state in x-ray photoelectron spectroscopy based on sample-work-function referencing to adventitious carbon: resolving the myth of apparent constant binding energy of the C 1s peak, *Appl. Surf. Sci.*, 2018, **451**, 99–103.

27 G. Greczynski and L. Hultman, C 1s peak of adventitious carbon aligns to the vacuum level: dire consequences for material's bonding assignment by photoelectron spectroscopy, *ChemPhysChem*, 2017, **18**, 1507–1512.

28 M. Podia and A. K. Tripathi, Role of shallow donor defects in inducing broad visible photoluminescence in ZnO thin film, *J. Lumin.*, 2025, **280**, 121083, DOI: **10.1016/j.jlumin.2025.121083**.

29 S. Farooq, R. Cai, J. McGettrick, E. Pean, M. Davies, A. S. Al Harrasi, R. Palmer and C. Tizaoui, Visible-light induced photocatalytic degradation of estrone (E1) with hexagonal copper selenide nanoflakes in water, *Process Saf. Environ. Prot.*, 2023, **172**, 1–15.

30 Y. Cheng, J. Zhang, X. Xiong, C. Chen, J. Zeng, Z. Kong, H. Wang, J. Xi, Y.-J. Yuan and Z. Ji, High photocatalytic and photoelectrochemical performances of the CuSe/MoSe$_2$ 2D/2D face-to-face heterojunction photocatalyst, *J. Alloys Compd.*, 2021, **870**, 159540, DOI: **10.1016/j.jallcom.2021.159540**.

31 K. Kaviyarasu, A. Ayeshamariam, E. Manikandan, J. Kennedy, R. Ladchumananandasivam, U. Umbelino Gomes, M. Jayachandran and M. Maaza, Solution processing of CuSe quantum dots: Photocatalytic activity under RhB for UV and visible-light solar irradiation, *Mater. Sci. Eng., B*, 2016, **210**, 1–9, DOI: **10.1016/j.mseb.2016.05.002**.

32 L. Gao, H. Ren, X. Lu, S. Woo Joo, T. Xiaoteng Liu and J. Huang, Heterostructure of NiSe$_2$/MnSe nanoparticles distributed on cross-linked carbon nanosheets for high-performance sodium-ion battery, *Appl. Surf. Sci.*, 2022, **599**, 154067, DOI: **10.1016/j.apsusc.2022.154067**.

33 K. Matras-Postołek, S. Sovinska and A. Węgrzynowicz, Synthesis and characterization of ZnSe and ZnSe: Mn nanosheets and microflowers with high photoactive properties by microwave-assisted method, *Chem. Eng. Process.*, 2019, **135**, 204–216, DOI: **10.1016/j.cep.2018.11.022**.

34 J. Tian, L. Lv, C. Fei, Y. Wang, X. Liu and G. Cao, A highly efficient (> 6%) Cd$_{1-x}$ Mn$_x$ Se quantum dot sensitized solar cell, *J. Mater. Chem. A*, 2014, **2**, 19653–19659.

35 H. Tan, C. Wang, W. Hu, H. Duan, P. Guo, N. Li, G. Li, L. Cai, Z. Sun, F. Hu and W. Yan, Reversible Tuning of the Ferromagnetic Behavior in Mn-Doped MoS$_2$ Nanosheets via Interface Charge Transfer, *ACS Appl. Mater. Interfaces*, 2018, **10**, 31648–31654, DOI: **10.1021/acsami.8b11623**.

36 P. Han, X. Zhang, C. Luo, W. Zhou, S. Yang, J. Zhao, W. Deng and K. Han, Manganese-Doped, Lead-Free Double Perovskite Nanocrystals for Bright Orange-Red Emission, *ACS Cent. Sci.*, 2020, **6**, 566–572, DOI: **10.1021/acscentsci.0c00056**.

37 M. Podia and A. K. Tripathi, Structural, optical and luminescence properties of ZnO thin films: Role of hot electrons defining the luminescence mechanisms, *J. Lumin.*, 2022, **252**, 119331, DOI: **10.1016/j.jlumin.2022.119331**.

38 T. Tauc, P. Kubelka, F. Munk, S. Information and T. Tauc, *How To Correctly Determine the Band Gap Energy of Modi fi ed Semiconductor Photocatalysts Based on UV-Vis Spectra*, 2018, pp. 8–11, DOI: **10.1021/acs.jpclett.8b02892**.

39 H. Chen, Y. Xing, S. Liu, J. Fu, H. Shi, Y. Liang, L. Wang and W. Wang, Efficient pollutant degradation under ultraviolet to near-infrared light irradiation and dark condition using CuSe nanosheets: Mechanistic insight into degradation, *J. Colloid Interface Sci.*, 2022, **613**, 103–116, DOI: **10.1016/j.jcis.2022.01.020**.

40 Y. Gu, Y. Su, D. Chen, H. Geng, Z. Li, L. Zhang and Y. Zhang, Hydrothermal synthesis of hexagonal CuSe nanoflakes with excellent sunlight-driven photocatalytic activity, *CrystEngComm*, 2014, **16**, 9185–9190, DOI: **10.1039/c4ce01470g**.

41 L. Han, L. Wu, C. Liu and J. Zhang, Doping-enhanced visible-light absorption of CH$_3$NH$_3$PbBr$_3$ by the Bi$^{3+}$-induced impurity band without sacrificing a band gap, *J. Phys. Chem. C*, 2019, **123**, 8578–8587.

42 U. P. Suryawanshi, U. V Ghorpade, P. V Kumar, J. S. Jang, M. He, H. J. Shim, H. R. Jung, M. P. Suryawanshi and J. H. Kim, Dopant induced hollow Ni$_2$P nanocrystals regulate dehydrogenation kinetics for highly efficient solar-driven hydrazine assisted H$_2$ production, *Appl. Catal., B*, 2024, **355**, 124165, DOI: **10.1016/j.apcatb.2024.124165**.

43 I. G. Shitu, Z. A. Talib, J. L. Y. Chi, M. M. A. Kechick and H. Baqiah, Influence of tartaric acid concentration on structural and optical properties of CuSe nanoparticles synthesized via microwave assisted method, *Results Phys.*, 2020, **17**, 1–12, DOI: **10.1016/j.rinp.2020.103041**.

44 M. Petrović, M. Gilić, J. Ćirković, M. Romčević, N. Romčević, J. Trajić and I. Yahia, Optical properties of CuSe thin films – band gap determination, *Sci. Sintering*, 2017, **49**, 167–174, DOI: **10.2298/SOS1702167P**.

45 K. Kaviyarasu, A. Ayeshamariam, E. Manikandan, J. Kennedy, R. Ladchumananandasivam, U. Umbelino Gomes, M. Jayachandran and M. Maaza, Solution processing of CuSe quantum dots: Photocatalytic activity under RhB for UV and visible-light solar irradiation, *Mater. Sci. Eng., B*, 2016, **210**, 1–9, DOI: **10.1016/j.mseb.2016.05.002**.

46 B. Barman, K. C. Handique, Y. Nanung and P. K. Kalita, Synthesis and characterization of chemically synthesized CuSe nanoparticles for photovoltaic application, *Mater. Today: Proc.*, 2019, **46**, 6213–6217, DOI: **10.1016/j.matpr.2020.04.658**.

47 M. Podia and A. K. Tripathi, Structural, optical and luminescence properties of ZnO thin films: Role of hot electrons defining the luminescence mechanisms, *J. Lumin.*, 2022, **252**, 119331, DOI: **10.1016/j.jlumin.2022.119331**.

48 J. Mooney and P. Kambhampati, Get the basics right: Jacobian conversion of wavelength and energy scales for quantitative analysis of emission spectra, *J. Phys. Chem. Lett.*, 2013, **4**, 3316–3318, DOI: **10.1021/jz401508t**.

49 I. G. Shitu, J. Y. C. Liew, Z. A. Talib, H. Baqiah, M. M. Awang Kechik, M. Ahmad Kamarudin, N. H. Osman, Y. J. Low and I. I. Lakin, Influence of irradiation time on the structural and optical characteristics of CuSe nanoparticles synthesized *via* microwave-assisted technique, *ACS Omega*, 2021, **6**, 10698–10708.

50 S. min Chang and W. szu Liu, The roles of surface-doped metal ions (V, Mn, Fe, Cu, Ce, and W) in the interfacial behavior of TiO$_2$ photocatalysts, *Appl. Catal., B*, 2014, **156–157**, 466–475, DOI: **10.1016/j.apcatb.2014.03.044**.

51 M. L. Liu, B. Bin Chen, R. S. Li, C. M. Li, H. Y. Zou and C. Z. Huang, Dendritic CuSe with Hierarchical Side-Branches: Synthesis, Efficient Adsorption, and Enhanced Photocatalytic Activities under Daylight, *ACS Sustainable Chem. Eng.*, 2017, **5**, 4154–4160, DOI: **10.1021/acssuschemeng.7b00126**.

52 C.-L. Tan, M.-Y. Qi, Z.-R. Tang and Y.-J. Xu, Superior Photoredox Coupling of Selective Ethanol Oxidation and CO$_2$ Reduction over ZnIn$_2$S$_x$@CeO$_x$ with Spatially Separated Redox Active Sites, *Artif. Photosynth.*, 2025, **1**, 144–155, DOI: **10.1021/aps.5c00005**.

53 Y. Zhang, L.-H. Gao, M.-Y. Qi, Z.-R. Tang and Y.-J. Xu, Cooperative photoredox coupling of CO$_2$ reduction with thiols oxidation by hybrid CdSe/CdS semiconductor quantum dots, *Appl. Catal., B*, 2025, **367**, 125118.

54 Y. He, M. Mei, Q. Yang, Y. Yang and Z. Ma, Covalently grafting porphyrin on SnO$_2$ nanorods for hydrogen evolution and tetracycline hydrochloride removal from real pharmaceutical wastewater with significantly improved efficiency, *Chem. Eng. J.*, 2023, **472**, 144859, DOI: **10.1016/j.cej.2023.144859**.

55 M. Tanveer, C. Cao, Z. Ali, I. Aslam, F. Idrees, W. S. Khan, F. K. But, M. Tahir and N. Mahmood, Template free synthesis of CuS nanosheet-based hierarchical microspheres: an efficient natural light driven photocatalyst, *CrystEngComm*, 2014, **16**, 5290–5300, DOI: **10.1039/c4ce00090k**.

56 J. Qu, Y. Yu, C. Y. Cao and W. G. Song, α-Fe$_2$O$_3$ nanodisks: Layered structure, growth mechanism, and enhanced photocatalytic property, *Chem.—Eur. J.*, 2013, **19**, 11172–11177, DOI: **10.1002/chem.201301295**.